

Band-filling Effects in Single-crystalline Oligomer Models for Doped PEDOT: 3,4-Ethylenedioxythiophene (EDOT) Dimer Salt with Hydrogen-bonded Infinite Sulfate Anion Chains

Ryohei Kameyama, Tomoko Fujino,* Shun Dekura, Shusaku Imajo, Tatsuya Miyamoto, Hiroshi Okamoto, and Hatsumi Mori*

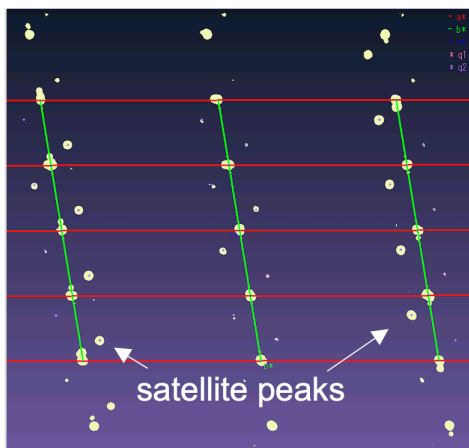
Table of Contents

| | |
|---|-----|
| 1. Single-crystal XRD structural analyses..... | S1 |
| 2. DFT calculations of donor molecule and bond length analyses..... | S5 |
| 3. Vibration Raman spectra analyses | S6 |
| 4. Overlap and transfer integrals calculations | S8 |
| 5. Crystal orbital and band structure calculations | S8 |
| 6. Electrical resistivity measurements | S9 |
| 7. Polarized reflectivity spectra analyses | S10 |
| 8. ESR measurements..... | S11 |
| 9. Static magnetic susceptibility measurements..... | S13 |
| 10. Thermoelectric power measurements..... | S13 |

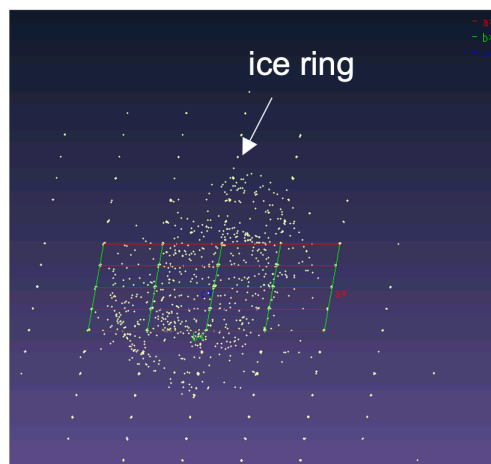
1. Single-crystal XRD structural analyses

Single-crystal XRD measurements were performed at 293 K and 150 K after cooling the sample by -2 K. Aside from the major reflections in the single crystal XRD at 293 K, two types of weak reflections were detected. Their d -spacings of the minor reflections were different from those of the commensurate superlattices or twinned crystals (Figure S1). The appearance of these satellite peaks suggests the coexistence of an incommensurate structure that may include incommensurately perioded lattice length within the ac -plane, originating either in the positional or structural modulation of hydrogensulfate anions or disordered solvents. These satellite peaks disappeared at 150 K as shown in Figure S1b, while the relatively high conductivity was maintained, indicating that the existence of the incommensurate structure observed at 293 K may not be related to the band-filling modulations.

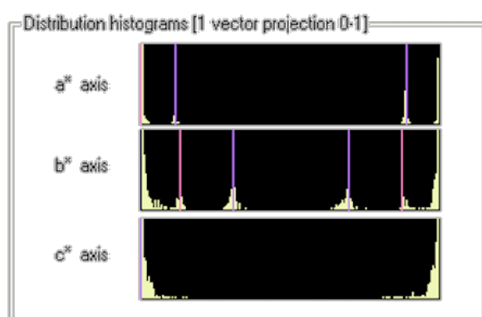
(a) 293 K



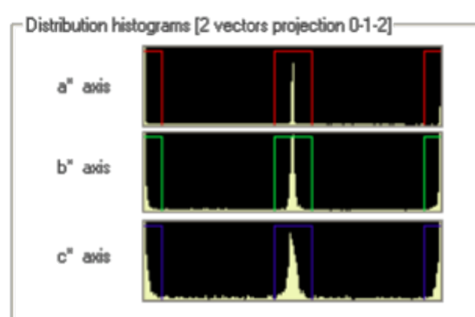
(b) 150 K



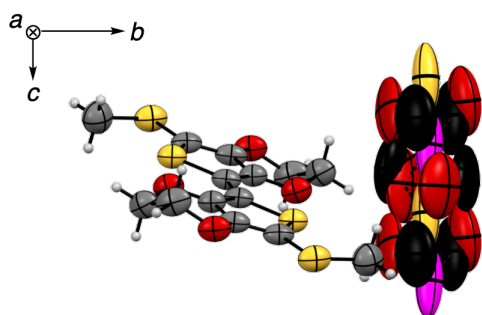
(c)



(d)



(e)



(f)

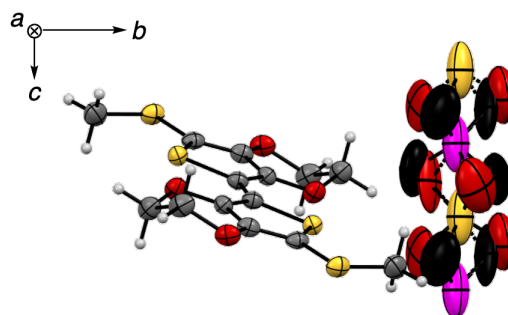


Figure S1. (a, b) X-ray diffraction patterns of a single crystal of **2O**-HSO₄ at 293 K (a) and 150 K (b), and the distribution histograms at 293 K (c) and 150 K (d). (e, f) Molecular structures in the single crystal of **2O**-HSO₄ in ORTEP drawings with 50% thermal ellipsoids at 293 K (e) and 150 K (f). Disordered S and O atoms in the anions were colored in yellow/red and pink/black. Other atoms were colored as follows; yellow: S atom; red: O atom; gray: C atom; white: H atom.

Table S1. Crystallographic data of a single crystal of **2O**–HSO₄ at 293 K and 150 K.

| Compounds | 2O –HSO ₄ | 2O –HSO ₄ |
|---|--|--|
| Temperature / K | 293 | 150 |
| Formula | C ₁₄ H ₁₄ O ₈ S ₅ ^a | C ₁₄ H ₁₄ O ₈ S ₅ ^a |
| Formula weight | 470.55 ^a | 470.55 ^a |
| Crystal system | <i>monoclinic</i> | <i>monoclinic</i> |
| Space group | <i>P2₁/c</i> (#14) | <i>P2₁/c</i> (#14) |
| <i>a</i> / Å | 10.8176(7) | 10.6718(6) |
| <i>b</i> / Å | 22.839(2) | 22.7325(12) |
| <i>c</i> / Å | 4.0259(3) | 3.9848(2) |
| <i>α</i> / deg. | 90 | 90 |
| <i>β</i> / deg. | 99.428(7) | 100.355(6) |
| <i>γ</i> / deg. | 90 | 90 |
| <i>V</i> / Å ³ | 981.21(14) | 950.95(9) |
| <i>Z</i> | 2 | 2 |
| <i>D</i> _{calc} / g cm ⁻³ | 1.593 ^a | 1.643 ^a |
| <i>R</i> _{int} | 0.0465 | 0.0502 |
| <i>R</i> ₁ (<i>I</i> > 2.00σ(<i>I</i>)) | 0.0685 | 0.0766 |
| <i>wR</i> ₂ (all reflections) | 0.1834 | 0.2117 |
| GOF | 1.017 | 1.074 |
| Residual electron density per donor from solvent mask analysis | 25 | 27 |
| Void volume per donor / Å ³ | 63 | 55 |
| CCDC | 2130644 | 2130652 |

^aIn the analyses, protons of the hydrogensulfate anions were omitted. Atoms of disordered solvent molecules were also excluded by a solvent-mask option implemented in Olex2. Therefore, formula, formula weight, and density correspond to the structures that excluded the protons and the solvent molecules.

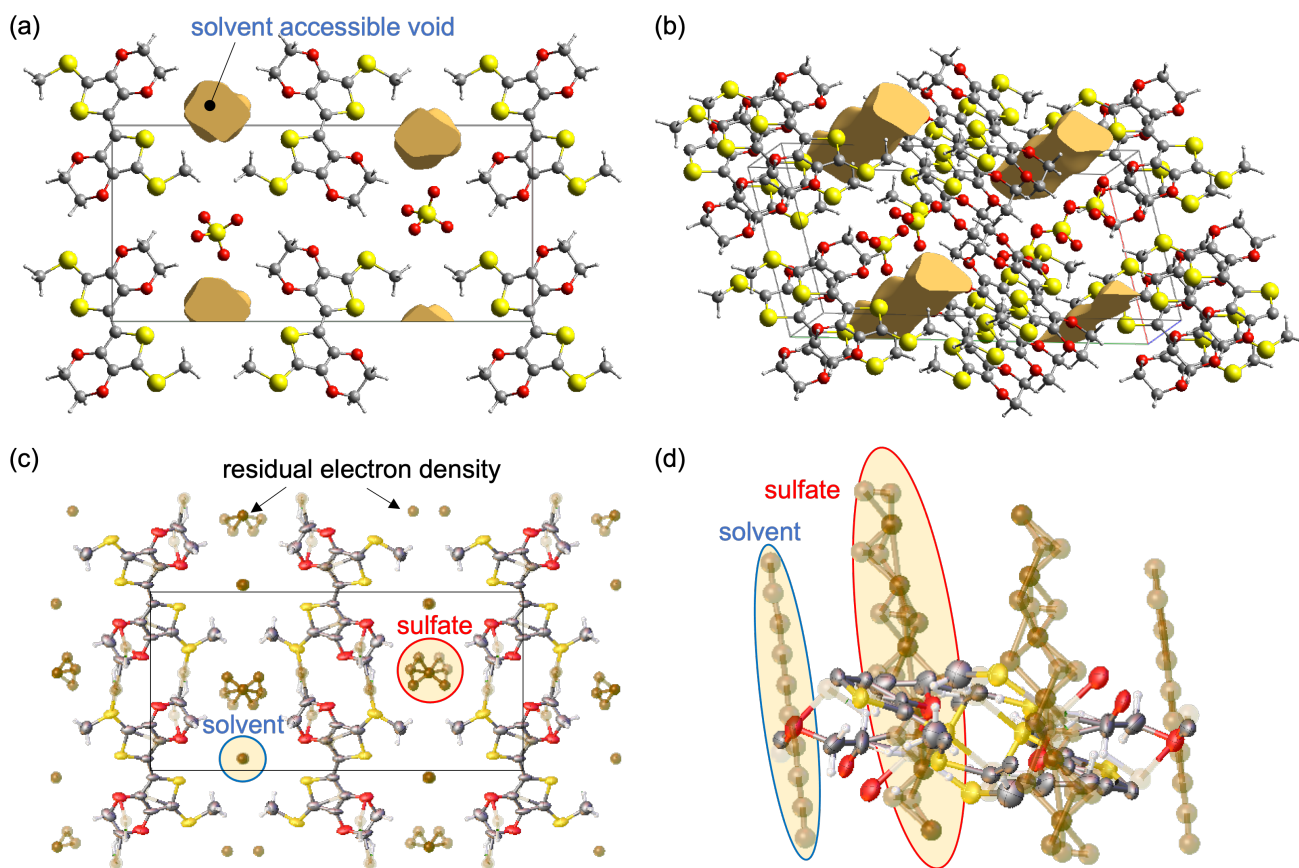


Figure S2. (a, b) Visualization of solvent-accessible voids in the single-crystal structures of **2O**-HSO₄ by Crystal Explorer software (ver. 17.5¹) from the viewpoints of the *c*-axis (a) and the direction slightly tilted from the *c*-axis (b). (c, d) Visualization of residual electron density except for the donor molecules **2O** detected in the XRD single-crystal structure analyses with Olex2,² along with **2O** shown in thermal ellipsoids (50%).

2. DFT calculations of donor molecule and bond length analyses

To estimate the charge transfer degree δ of **2O**–HSO₄ single crystal from the bond length analyses, we simulated the bond length change upon oxidation of a neutral donor **2O** ($\delta = 0$), through a radical cation ($\delta = 1$; **2O^{•+}**), to a dication ($\delta = 2$; **2O²⁺**) by DFT calculations with gaussian16 (g16, (U)B3LYP 6-31G^{*}(d)).³ The values of " $(a+c)/b$ " with the lengths of C–C bonds (a – d , Figures 3b and S3d) in the optimized structures for **2O**, **2O^{•+}**, and **2O²⁺** showed a good linearity to δ (Figure S3e), representing an equation: $\delta = -29.802 + 15.385*(a+c)/b$. The reliability of the equation was supported by the single-crystal structural data of **2O** with non-charged donor and **2O^{•+}** $\cdot X$ ($X = \text{BF}_4, \text{ClO}_4, \text{PF}_6$) with the +1-charged donor. The calculated $(a+c)/b$ value for **2O** (1.92) estimates δ to be -0.20 ± 0.05 , and the values for **2O^{•+}** $\cdot X$ (1.99–2.02) estimate δ to be 0.89 ± 0.09 for **2O^{•+}** $\cdot \text{BF}_4$, 1.12 ± 0.07 for **2O^{•+}** $\cdot \text{ClO}_4$, and 1.28 ± 0.08 for **2O^{•+}** $\cdot \text{PF}_6$, indicating that δ for +1-charged donor ranged from 0.9–1.3. The $(a+c)/b$ value for **2O**–HSO₄ was calculated to be 2.02 that estimates δ to be 1.2 ± 0.1 , suggesting the donor valency is close to +1.

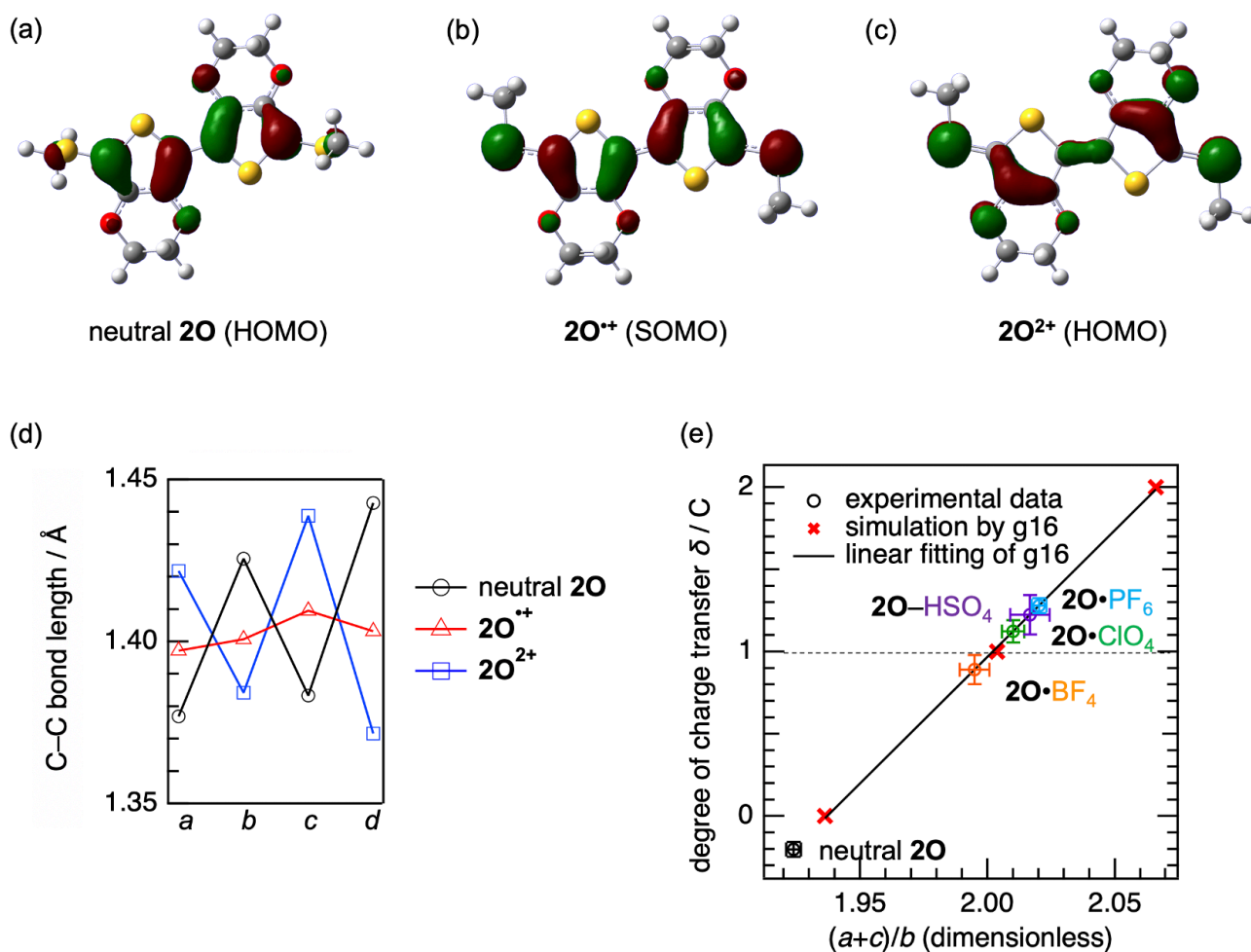


Figure S3. (a–d) DFT-calculated molecular orbitals of a **2O** donor: HOMO of **2O** (a), SOMO of **2O^{•+}** (b), and HOMO of **2O²⁺** (corresponding to HOMO–1 of **2O**) (c), respectively and the simulated C–C bond lengths (d). (e) The relationship between the $(a+c)/b$ value from the bond lengths and δ . The solid line is a fitting curve for g16-simulated values: $\delta = -29.802 + 15.385*(a+c)/b$.

3. Vibration Raman spectra analyses

The vibration Raman spectra of single crystals of **2O**, **2O**·*A* (*A* = BF₄, ClO₄, and PF₆), and **2O**-HSO₄ were measured upon irradiation of a 532 nm-pulse laser at 293 K (Figure S4a). The observed signals were analyzed by peak fittings using a sum of Lorentzian peaks (e.g., Figure S4c for **2O** and Figure S4d for **2O**-HSO₄), and each peak was assigned according to the simulated Raman spectra by the optimized structures based on g16 (U)B3LYP, 6-31G*(d) (Figure S4b, Table S2). The spectrum of **2O**-HSO₄ was similar to those of **2O**·*A*, suggesting that the δ was close to 1, as was supported by the bond length analyses (Figures 3c, S3).

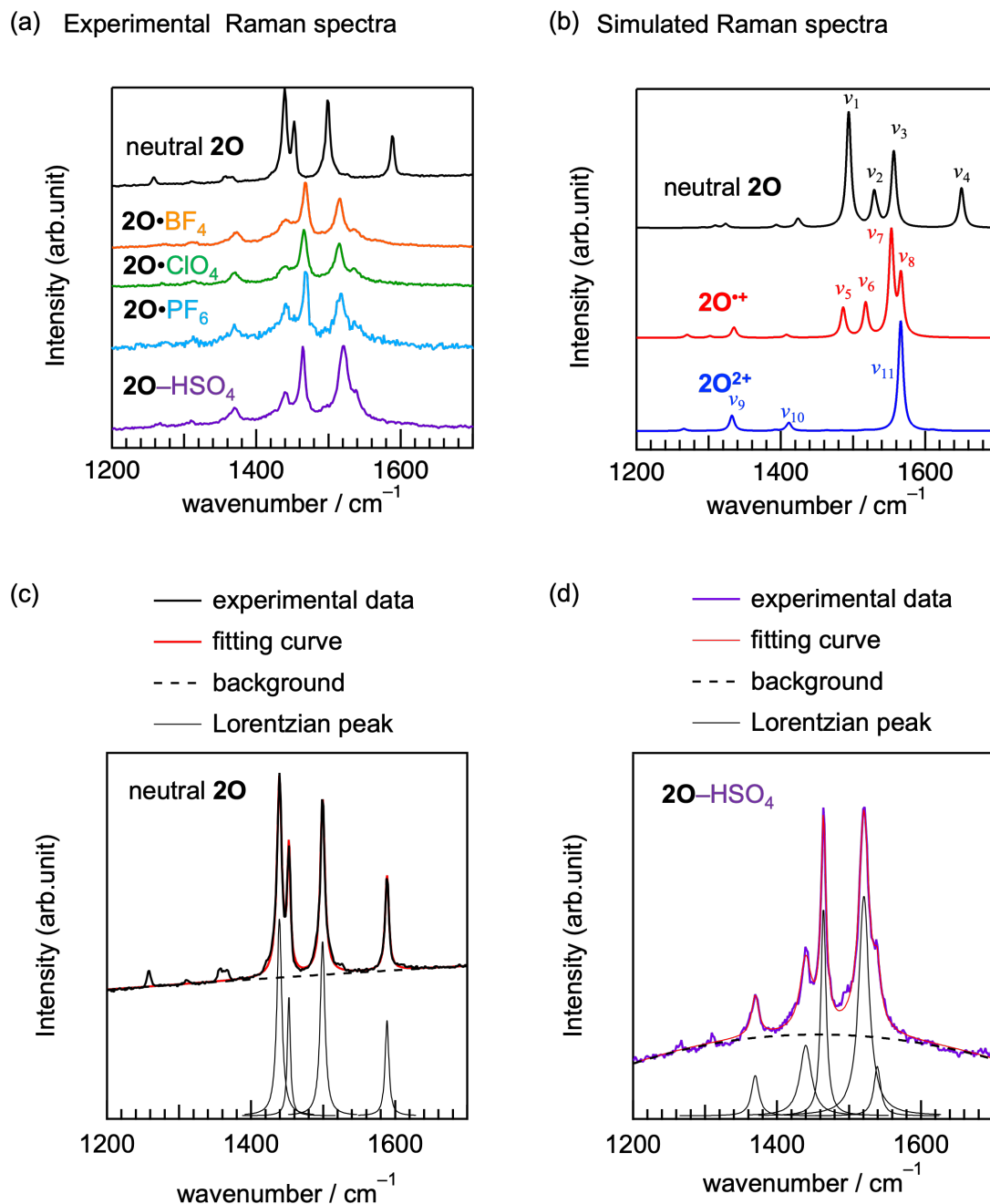


Figure S4. (a, b) Experimental Raman spectra (a) and the simulated spectra (b) of neutral **2O**, **2O**·*A* (*A* = BF₄, ClO₄, and PF₆), and **2O**-HSO₄ measured by irradiation of a 532 nm-pulse laser at 293 K. (c, d) Peak fitting of experimental data with a sum of Lorentzian peaks for neutral **2O** (c) and **2O**-HSO₄ (d).

Table S2. Peak assignment of Raman spectra (s: strong, m: moderate, w: weak).

| Compound | Observed signals (cm ⁻¹) |
|--|---------------------------------------|
| 2O | 1439.01±0.03 (s) |
| | 1452.28±0.04 (m) |
| | 1499.03±0.04 (s) |
| | 1588.45±0.06 (m) |
| 2O•BF₄ | 1444.0±0.5 (m) |
| | 1468.09±0.05 (s) |
| | 1514.82±0.09 (s) |
| | 1537.8±0.4 (w) |
| 2O•ClO₄ | 1440.13±0.33 (m) |
| | 1465.81±0.06 (s) |
| | 1514.19±0.10 (s) |
| | 1537.38±0.43 (w) |
| 2O•PF₆ | 1440.7±1.0 (m) |
| | 1468.5±0.1 (s) |
| | 1516.1±0.3 (s) |
| | 1531.1±3.0 (w) |
| 2O–HSO₄ | 1439.66±0.30 (m) |
| | 1464.35±0.07 (s) |
| | 1520.49±0.11 (s) |
| | 1539.05±0.35 (w) |
| Compound | Simulated signals (cm ⁻¹) |
| 2O (optimized structure)^a | 1470.30 (s) ν_1 |
| | 1508.52 (m) ν_2 |
| | 1535.76 (s) ν_3 |
| | 1629.65 (m) ν_4 |
| 2O⁺ (optimized structure)^a | 1486.19 (w) ν_5 |
| | 1517.40 (w) ν_6 |
| | 1553.00 (s) ν_7 |
| | 1566.37 (m) ν_8 |
| 2O²⁺ (optimized structure)^a | 1332.15 (w) ν_9 |
| | 1411.08 (w) ν_{10} |
| | 1565.99 (s) ν_{11} |

^a The chemical structure is optimized with Gaussian 16 Revision C.01.³

4. Overlap and transfer integrals calculations

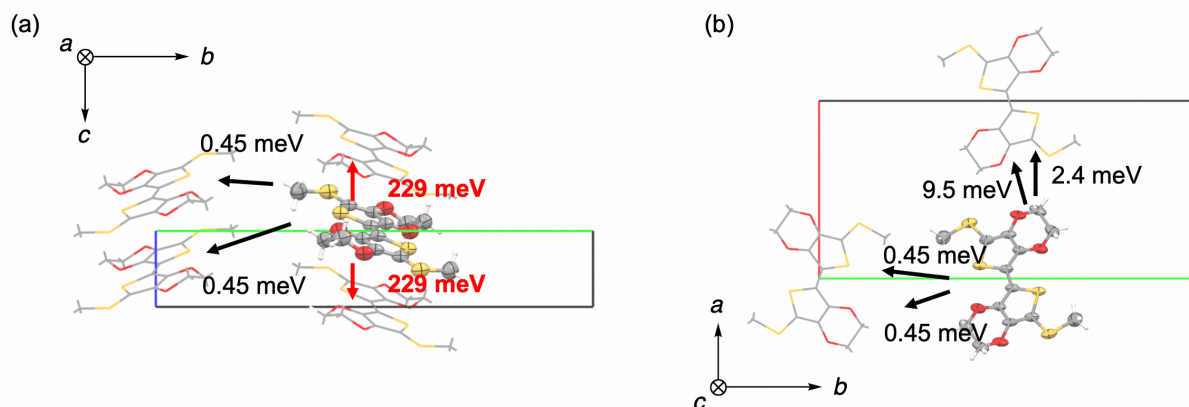


Figure S5. Transfer integrals of 2O-HSO_4 between a donor and one of the six nearest neighboring donors. Views were shown along the a -axis (a) and the c -axis (b), respectively.

5. Crystal orbital and band structure calculations

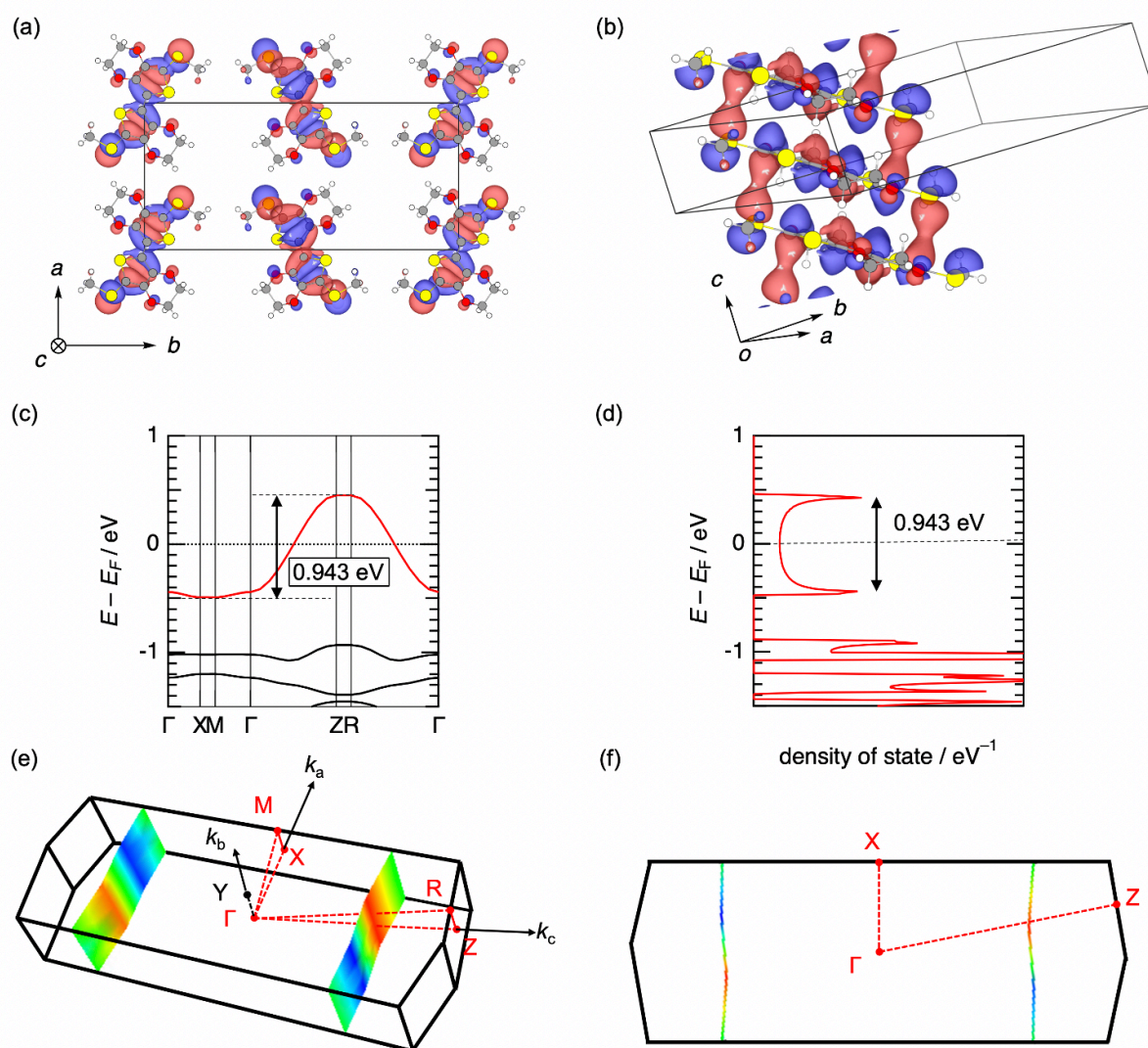


Figure S6. Crystal orbital and band structure of 2O-HSO_4 . The charge for each donor molecule was set to be $+1.0$. (a, b) The real parts of the highest-occupied crystal orbital (HOCO) at the Γ point (0,0,0). The parts were visualized

by VESTA⁴ along the c -axis (a) and π -plane (b). (c) Band structure and (d) density of states calculated by OpenMX. (e, f) The Fermi surface (color change corresponding to the Fermi velocity) and the first Brillouin zone of **2O**-HSO₄ generated by FermiSurfer.⁵ (f) A cross-section of the Fermi surface and the first Brillouin zone from the perpendicular to the k_b direction.

6. Electrical resistivity measurements

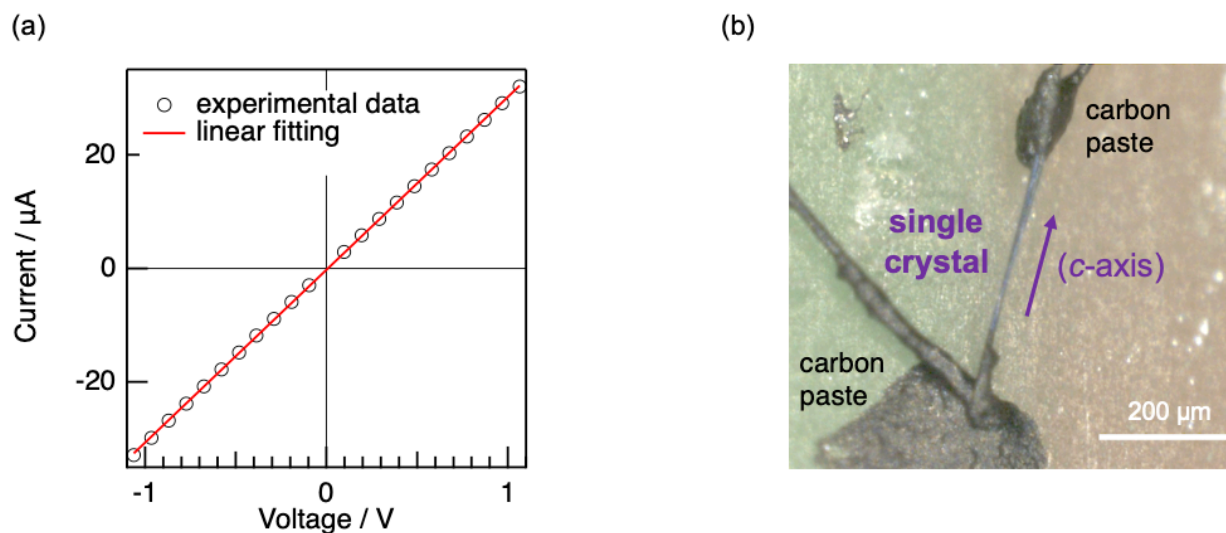


Figure S7. (a) I - V curve of **2O**-HSO₄ at 293 K. The inset is a single crystal of **2O**-HSO₄ used for the conductivity measurement. (b) A picture of a single crystal used in the measurement.

From the estimation of δ of **2O**-HSO₄ to be close to +1 by bond lengths analyses in single crystals and the Raman spectra analyses, we can propose two possible electronic states of **2O**-HSO₄: " $\delta = +1$ " or " $\delta \approx +1$ ($\delta \neq +1$)."

Assuming the electronic state of " $\delta = +1$ " where the band filling of the system is exactly "half-filled", an extended Hubbard model⁶ can be applied. Under the model, U_{eff} can be expressed as $U - 2V$, where U and V represent intramolecular and nearest intermolecular Coulomb repulsion, respectively. The U of **2O**-HSO₄ was equal to those of **2O**•*A* because of the use of the identical donor (**2O**), whereas V of **2O**-HSO₄ was estimated to be smaller compared to those of **2O**•*A* owing to the extended central distances between donors (Table 1, Figures 2c and 2d). Consequently, $U_{\text{eff}} (= U - 2V)$ of **2O**-HSO₄ was expected to be larger than those of **2O**•*A*. However, the prediction is contradictory to the estimation of U_{eff} from the experimental results with a single crystal of **2O**-HSO₄; a combination of the determined smaller activation energy E_a and smaller W compared to those of **2O**•*A* indicated a smaller U_{eff} according to the following equation used in the extended Hubbard model: $U_{\text{eff}} = W + 2E_a$. Therefore, the assumption of " $\delta = +1$ (half-filled electronic state)" was rejected and supported the electronic state of $\delta \approx +1$ ($\delta \neq +1$) in which the band filling is deviated from the half-filling. The decrease of U_{eff} was supported by the optical conductivity data (Figures 6b, S8 and S9).

7. Polarized reflectivity spectra analyses

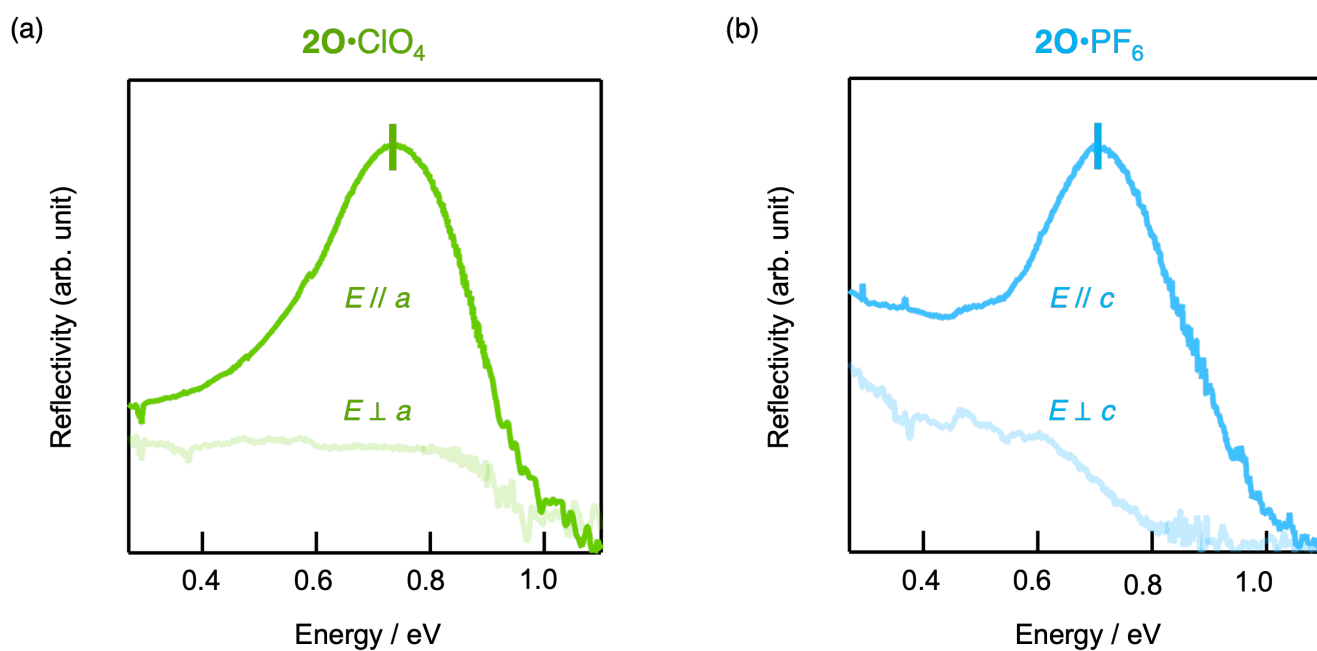


Figure S8. Polarized reflectivity spectra for single crystals of $2\mathbf{O}\cdot\text{ClO}_4$ (a) and $2\mathbf{O}\cdot\text{PF}_6$ (b), measured with the electric field of the light (E) parallel (\parallel) and perpendicular (\perp) to the π -stacking directions. Bars indicate the peak tops for the spectra obtained by applying E parallel to the π -stacking directions.

8. ESR measurements

All the spectra were analyzed by fitting a sum of two symmetrical Lorentzian curves, mainly due to the two types of π -stacking columns rotating along the stacking direction (the c -axis) in a cell of the single crystal. The spectra at $\varphi = 0^\circ$ showed the simplest curve like a Lorentzian curve with a peak-to-peak width ΔB_{pp} of ~ 0.5 G, and the signals at the angle were measured from 290 K to 4 K (Figures S9c–e). The spin susceptibility χ_{spin} was calculated by the following equation:

$$\chi_{spin} \propto I_m \times (\Delta B_{pp})^2$$

, where maximum intensity I_m , the peak-to-peak width ΔB_{pp} and resonance center B_0 were determined by fitting to the equation of Lorentzian in the differential form as follows:

$$I(B) = a \times \frac{16 \times I_m \times (B_0 - B) / (\Delta B_{pp} / 2)}{[3 + \{\frac{B_0 - B}{\Delta B_{pp}} / 2\}^2]^2} + b \times \frac{16 \times I'_m \times (B'_0 - B) / (\Delta B'_{pp} / 2)}{[3 + \{\frac{B'_0 - B}{\Delta B'_{pp}} / 2\}^2]^2}$$

. The spectra showed a thermal hysteresis; upon cooling, the spin susceptibility (χ_{spin}) calculated from the spectrum shape was decreased below ca. 200 K (Figure S10d), along with the increase of the ΔB_{pp} , indicating a transition to the paramagnetic to the non-magnetic state. The demagnetization may correspond to a spin-Peierls-like transition, as have been observed in **2O•A**. The singlet–triplet (S–T) gap ($2|J|/k_B$) was estimated by fitting the spin susceptibility to the cooling curve using an equation:

$$\chi_{spin} \approx \frac{Ng^2\mu_B^2}{k_B T} \frac{1}{3 + \exp \frac{2|J|}{k_B T}}$$

. The $2|J|/k_B$ value was estimated to be 763 ± 25 K (fitted between 100–220 K with a constant background, Figure S9d). The relatively small $2|J|/k_B$ value compared to **2O•A** (~ 1000 K) implies the decrease of t for intracolumnar orbital interaction of donors compared to those in **2O•A** according to the following relationship:

$$\frac{2|J|}{k_B} \sim \frac{t^2}{U}$$

. The implication supports the smaller intracolumnar t values for **2O**–HSO₄ from ADF calculations (Table 1, Figure S5).

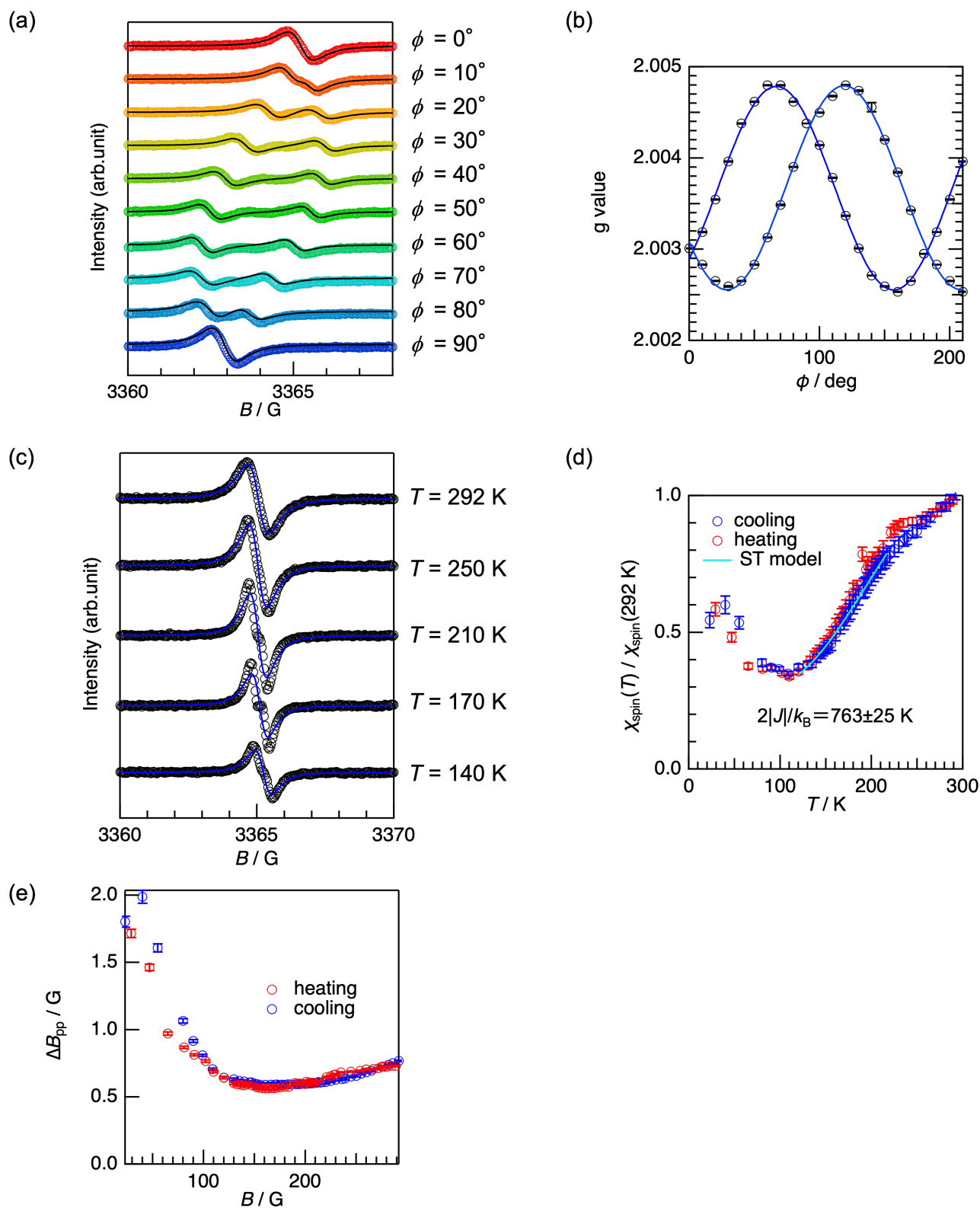


Figure S9. ESR spectra of 2O-HSO₄. (a) ϕ -dependent spectra at 292 K. Solid lines denote double Lorentzian curves used for the peak fitting. (b) ϕ -dependent g values in the spectra at 292 K. Blue solid lines denote fitting curves using an equation: $A\cos^2(\phi - \delta_1) + B\cos^2(\phi - \delta_2) + C$. (c) T -dependent spectra at $\phi = 0^\circ$. (d) T -dependent relative χ_{spin} upon cooling from 292 K to 23 K. The value was normalized by the value at 292 K. A green line denotes a fitting curve using a singlet-triplet (ST) model function. (e) T -dependent ΔB_{pp} upon cooling and subsequent heating.

9. Static magnetic susceptibility measurements

The static magnetic susceptibility of poly-crystalline samples of **2O**-HSO₄ was measured applying the static magnetic field of 10,000 Oe upon cooling the sample from 300 K to 50 K by 2 K/min, 49 K to 10 K by 1 K/min and 10 K to 2 K by 0.5 K/min. The absence of ferromagnetic impurity in the synthesized samples was confirmed from the obtained $M-H$ curve at 2 K around $-55,000$ to $55,000$ Oe. The magnetic susceptibilities (χ_{exp}) were corrected by subtracting the contribution of the Curie impurity for $S = 1/2$ (χ_{CW} ; 0.57 % for the molar amount of **2O**•HSO₄•H₂O: based on the elemental analysis) and the contribution from core diamagnetism ($\chi_{\text{core}} = 2.728 \times 10^{-4}$ emu mol⁻¹) estimated from Pascal's law⁷ (i.e., χ_p in Figure S10). The paramagnetic-to-demagnetization transition around 200 K upon cooling was consistent with the ESR analysis (Figure S9d). The anomaly around 50 K is attributed to the presence of molecular oxygen in the sample holder.

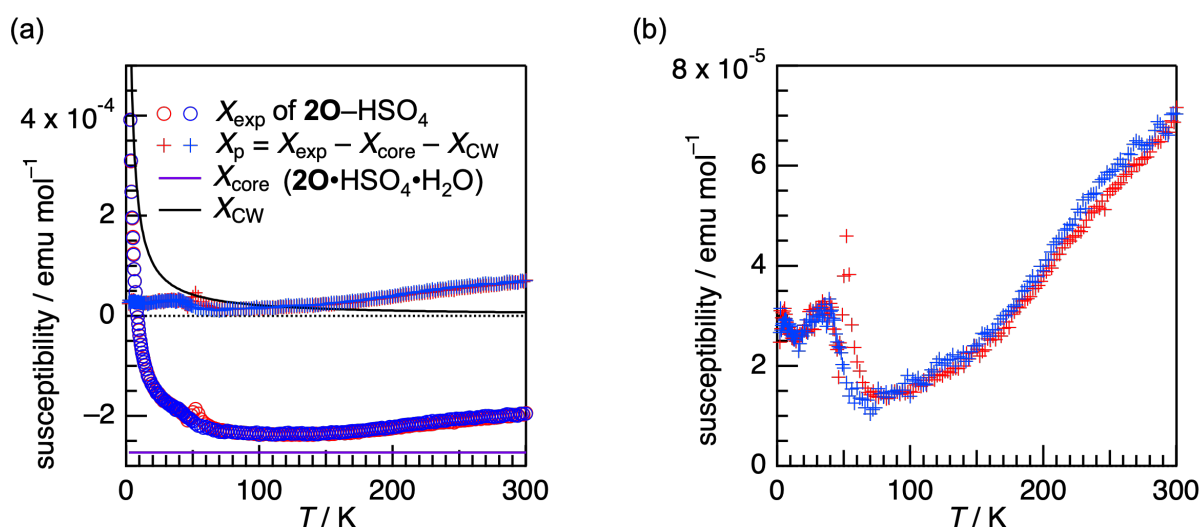


Figure S10. (a) $\chi-T$ plot for **2O**-HSO₄ measured for the polycrystalline sample under the static magnetic field of 10,000 Oe. (b) The enlarged χ_p-T plots of **2O**-HSO₄.

10. Thermoelectric power measurements

Thermoelectric power of **2O**-HSO₄ single crystal was measured along the long crystal axis (i.e., the π -stacking direction of donors) around room temperature. Thus, a single crystal was set on copper blocks and connected to a nanovoltmeter by attaching two gold wires at the termini by conductive carbon paste (Figure S11a). The generated voltage (thermoelectric power, ΔV) was measured by a nanovoltmeter upon heating the sample with a chip resistor, monitoring the temperature difference (ΔT). From the linear region of $\Delta V-\Delta T$ plot, the Seebeck constant S was estimated following $\Delta S = \Delta V/\Delta T$ to be $+(0.14 \pm 0.02)$ mV K⁻¹. On the other hand, the control half-filled **2O**•BF₄ and **2O**•ClO₄ single crystals that theoretically represented zero constants based on the tight-binding model also showed positive values: $+0.63(1)$ mV K⁻¹ and $+0.98(6)$ mV K⁻¹, respectively (Figure S11b). The positive values may originate in the asymmetric HOCO and LUCO (lowest unoccupied crystal orbitals) bands in their curvatures near the Van Hove singularity, leading to an effective mass difference between holes and electrons.⁸ It is noted that **2O**•PF₆ reached the detection limit because of the relatively large electrical noise derived from its high resistance. These data still make it controversial to determine the signatures of the Seebeck constant for the **2O**-HSO₄ single crystal. We plan to determine the doping direction from the half by increasing the deviation degree by additional chemical modifications.

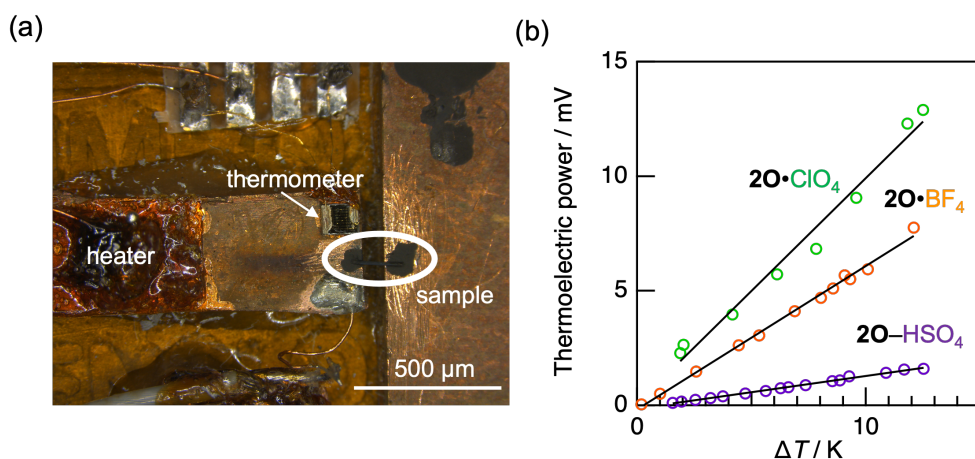


Figure S11. (a) A sample setup used for the thermoelectric power measurement in this study. (b) ΔV - ΔT plot of the single-crystals of **2O**-HSO₄, **2O**-BF₄, and **2O**-ClO₄ around room temperature. Solid lines denote linear fittings.

1. P. R. Spackman, M. J. Turner, J. J. McKinnon, S. K. Wolff, D. J. Grimwood, D. Jayatilaka and M. A. Spackman, *J. Appl. Cryst.*, 2021, **54**, 1006–1011.
2. O. V. Dolomanov, L. J. Bourhis, R. J. Gildea, J. A. K. Howard and H. Puschmann, *J. Appl. Cryst.*, 2009, **42**, 339–341.
3. Gaussian 16, Revision C.01, M. J. Frisch, G. W. Trucks, H. B. Schlegel, G. E. Scuseria, M. A. Robb, J. R. Cheeseman, G. Scalmani, V. Barone, G. A. Petersson, H. Nakatsuji, X. Li, M. Caricato, A. V. Marenich, J. Bloino, B. G. Janesko, R. Gomperts, B. Mennucci, H. P. Hratchian, J. V. Ortiz, A. F. Izmaylov, J. L. Sonnenberg, D. Williams-Young, F. Ding, F. Lipparini, F. Egidi, J. Goings, B. Peng, A. Petrone, T. Henderson, D. Ranasinghe, V. G. Zakrzewski, J. Gao, N. Rega, G. Zheng, W. Liang, M. Hada, M. Ehara, K. Toyota, R. Fukuda, J. Hasegawa, M. Ishida, T. Nakajima, Y. Honda, O. Kitao, H. Nakai, T. Vreven, K. Throssell, J. A. Montgomery, Jr., J. E. Peralta, F. Ogliaro, M. J. Bearpark, J. J. Heyd, E. N. Brothers, K. N. Kudin, V. N. Staroverov, T. A. Keith, R. Kobayashi, J. Normand, K. Raghavachari, A. P. Rendell, J. C. Burant, S. S. Iyengar, J. Tomasi, M. Cossi, J. M. Millam, M. Klene, C. Adamo, R. Cammi, J. W. Ochterski, R. L. Martin, K. Morokuma, O. Farkas, J. B. Foresman and D. J. Fox, Gaussian, Inc., Wallingford CT, 2016.
4. K. Momma and F. Izumi, *J. Appl. Cryst.*, 2011, **44**, 1272–1276.
5. M. Kawamura, *Comput. Phys. Commun.*, 2019, **239**, 197–203.
6. J. Hubbard, *Proc. R. Soc. London, Ser. A*, 1963, **276**, 238–257.
7. G. A. Bain, J. F. Berry, *J. Chem. Educ.*, 2008, **85**, 532–536.
8. L. Van Hove, *Phys. Rev.* 1953, **89**, 1189–1193.